

**Complementary stabilization by core/sheath carbon
nanofibers/spongy carbon on submicron tin oxide particles
as anode for lithium-ion batteries**

Hongmei Ji,[†] Chao Ma,[†] Jingjing Ding,[†] Jie Yang,[†] Gang Yang,^{*,†} Yimin Chao,^{*,§}
Yang Yang[†]

[†] Jiangsu Laboratory of Advanced Functional Materials, Department of Chemistry,
Changshu Institute of Technology, Changshu 215500, P. R. China.

[§] Energy Materials Laboratory, School of Chemistry, University of East Anglia,
Norwich NR4 7TJ, UK

*Corresponding Author

E-mail: gyang@cslg.edu.cn (G. Yang)

Hongmei Ji and Chao Ma contributed to the work equally and should be regarded as
co-first authors.

Abstract: To limit the pulverization of tin-based anode materials during lithiation/delithiation, submicron tin oxide/tin particles are fixed on core/sheath carbon nanofiber/spongy carbon via hydrothermal and carbothermal reduction treatment in this work. During carbothermal reduction, SnO₂ nanosheets are converted to spherical Sn submicron particles and simultaneously the hollow spongy carbon is produced and still enwrap on carbon nanofiber. The as-produced flexible film is used for a binder-free anode for lithium ion batteries, without the polymer binder and conductive carbon. At 0.1, 0.5, 1 and 2 A g⁻¹, the composite electrode respectively displays a discharging capacity of 1393.0, 738.2, 583.6 and 382.6 mAh g⁻¹. Moreover, it delivers specific capacity of 726.9 mAh g⁻¹ and coulombic efficiency of 99.45 % after 300 cycles at 0.1 A g⁻¹. The comparison sample of carbon nanofiber/SnO_x film without the presence of spongy carbon displays much lower rate performance and worse cyclic performance. The integrated structure of carbon nanofiber/SnO_x/spongy carbon results in the remarkable Li-storage performance, in which the carbon nanofiber and spongy carbon synergistically provide conductive channel and buffer zone to hinder the pulverization and peeling of SnO_x particles during charging-discharging processes.

Keywords: Hybrid materials; Integrated structure; Cyclic performance; Charge transport; Structure-property relationships.

1. Introduction

Tin-based materials with abundant availability, environmental friendliness, and high theoretical capacity (Sn: 990 mA h g⁻¹; SnO₂: 780 mAh g⁻¹), have been attracted widely attention as anode materials for high-performance lithium-ion batteries (LIBs).¹⁻⁴ Nevertheless, the practical implementation of tin-based anodes (SnO_x) for LIBs is limited by huge volume expansion which results in the unavoidable cracking of solid electrolyte interphase (SEI), pulverization and the subsequent poor cycling performance.^{5,6}

Nanosized SnO_x and its hybrids with carbonaceous materials, such as carbon nanotubes, graphene, amorphous carbon and carbon nanofibers (CNF), have been extensively investigated to solve the problem of capacity fading.⁷⁻¹⁰ Nanosized particles can alleviate the volumetric change to some extent, but the nanoparticles result in serious side reaction and aggregation during charging/discharging.^{11,12} Among the carbonaceous materials, CNF as conductive additive and elastic buffer substrate has been effectively improved the electrochemical properties of metal oxides as anode materials for LIBs.^{13,14} Electrospinning followed by subsequent carbonization is a typical industrial method to produce CNF.¹⁵ In the previous publications, the precursors of tin salt and polyacrylonitrile are together electrospun and converted to SnO_x/CNF in-situ.^{16,17} SnO_x nanoparticles encapsulated in CNF present enhanced electrochemical properties, because the elastic nanofibers improve the stability and conductivity. However, for maintaining the flexibility of composite film it must contain less ratio of metal oxide with the aforementioned one-step method. Our group once reported the relationship between the film flexibility and the proportion of metal oxides, the over weight ratio of metal oxide in the composite causes new technical challenges for electrospinning with consequences of fiber

breakage and losing the flexibility.¹⁸ Recently, two-step method has been used for preparation the composite in which CNF supported metal oxides efficiently resolve the aforementioned problems.²⁴⁻²⁶ In our recent work, we reported a three dimensional network in which carbon coated SnO₂ micron-sized particles are fixed in carbon nanofibers (CNF/SnO₂@C). However, the seriously volume change observed in the sample decreases the cyclic performance of the composite sample.²⁷ By using pure CNF as substrate, metal oxide particles with more than 70wt% of the composite could be grown on the CNF network under hydrothermal condition and the film is still flexible. Moreover, the crystal morphology of metal oxides and the interface between CNF and metal oxides could be easily adjusted by the reaction parameters in hydrothermal system.²²

In this work, we synthesize a novel composite structure that the submicron tin oxide particles are fixed on core/sheath carbon nanofibers/spongy carbon (CNF/SnO_x/SC) through hydrothermal and carbothermal reduction method. CNF/SnO_x/SC flexible film as a binder-free anode is directly assembled in the LIB, without polymer binder and conductive carbon. CNF network confines submicron SnO_x particles, meanwhile, provides fast and continuous conductive channel. The spongy carbon efficiently suppresses SnO_x pulverization and promotes the electrons transfer capability of the composite film. Moreover, the synergy effect between the CNF and spongy carbon buffers the volumetric change of SnO_x and enhances the Li⁺ diffusion rate during lithiation/delithiation processes, and thus, CNF/SnO_x/SC possesses excellent rate performance and long term cycle stability.

2. Experimental Section

Stannous chloride dehydrate (SnCl₂·2H₂O), trisodium citrate dihydrate (Na₃C₆H₅O₇·2H₂O) and lithium hydroxide (LiOH) were used without further

purification. The starting CNF film as conductive substrate was prepared by electrospinning and carbonization according to the previous publications.^{15,22} In a typical procedure, polyacrylonitrile (PAN) was dissolved in N, N-dimethylformamide (DMF) and the solution produced PAN white film by electrospinning. The PAN film was preoxidized at 250 °C in air atmosphere, and then carbonized in a tube furnace at 700 °C in N₂ atmosphere to obtain black colored CNF film. The overall synthetic procedure of CNF/SnO_x and CNF/SnO_x/C flexible film was illustrated in Figure S1 (in Supporting Information). After the first hydrothermal process, CNF/SnO₂ flexible film was produced.

One batch of CNF/SnO₂ film was directly treated at high temperature under N₂ atmosphere to produce the flexible film of CNF/SnO_x. The other batch of CNF/SnO₂ film with glucose were together reacted in hydrothermal process again. Herein, spongy carbon (SC) was grown on the surface of CNF/SnO₂ to produce CNF/SnO₂/SC flexible film. The as-produced CNF/SnO₂/SC film was heat-treated under N₂ atmosphere. During the heat treatment of CNF/SnO₂ and CNF/SnO₂/SC films, SnO₂ was carbothermally reduced to spherical tin particles through the reaction ($\text{SnO}_2 + \text{C} \rightarrow \text{Sn} + \text{CO}_n$). The metallic tin surface grew a passivation layer once exposed to air atmosphere, and thus, the final products are respective CNF/SnO_x and CNF/SnO_x/SC flexible films (in the following, Sn coated by SnO₂ is simplified noted as SnO_x). The comparison sample SnO_x/C powder was synthesized through hydrothermal carbon coating and heat-treatment but without the CNF supporting.

The crystal structure of the samples were evaluated using X-ray powder diffractometer (XRD, Rigaku, Cu K α radiation). The thermal behaviors of samples was recorded by thermogravimetric analysis and differential scanning calorimetry (TG/DSC) under O₂ atmosphere at the temperature range from 50 to 900 °C. The

element weight ratio in sample was collected by Energy-dispersive X-ray spectroscopy and CHN elemental analysis (PerkinElmer 2400). The surface morphologies of samples were observed by scanning electron microscope (SEM, ZEISS SIGMA), and their microstructures were observed by transmission electron microscope (TEM) and high-resolution TEM (JEOL JEM-200CX). The valence states of the surface elements were acquired using X-ray photoelectron spectroscopy (XPS, Thermo Fisher Scientific, Escalab250Xi).

The as-produced composite films were directly applied as binder-free electrodes for LIBs. The electrochemical characterizations were accomplished using CR 2016 coin cells including Li foils as counter electrode, Celgard 2400 microporous films as separator, and 1 M LiPF₆ in dimethyl carbonate (DMC) and ethylene carbonate (EC) as electrolyte (1:1 volume mixture). The cells were assembled in an Ar-filled glove box in which the O₂ and H₂O contents were maintained at below 0.1 ppm. Cyclic voltammogram (CV) profiles were recorded at a scan rate of 0.1 mV s⁻¹ in the range of 0.001-2.5 V (CHI660E, Shanghai, China). Galvanostatic discharging and charging at various current rates were investigated in the voltage range of 0.001-3.0 V (LAND CT2001A battery testing system, Wuhan, China). Electrochemical impedance spectroscopy (EIS) measurements were recorded using PARSTAT2273 electrochemical workstation in the frequency range of 10⁻² Hz to 10⁵ Hz and voltage amplitude was 5 mV.

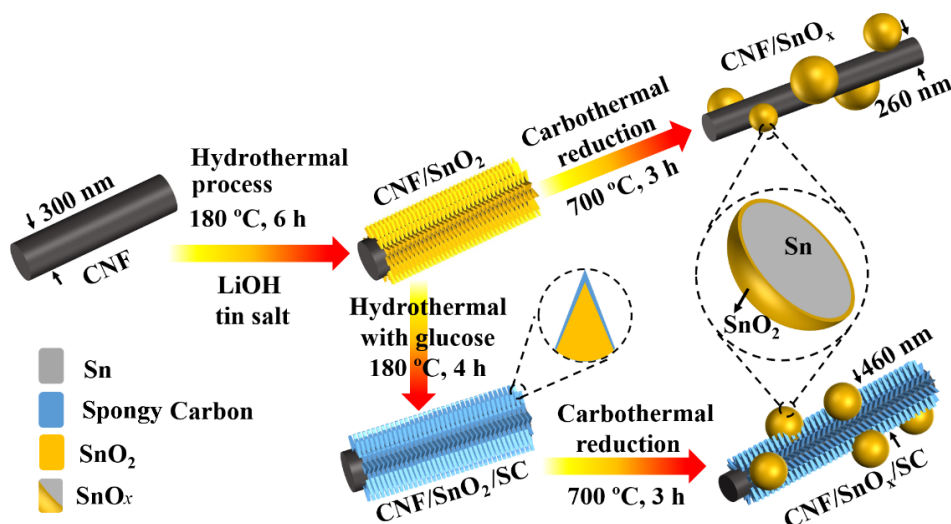


Figure 1. The illustration of the preparation route and microstructure for CNF/SnO₂, CNF/SnO₂/SC, CNF/SnO_x and CNF/SnO_x/SC.

3. Results and Discussion

3.1 Structure and Morphology of Hybrid Composites

Figure 1 represents the schematic preparation route for CNF/SnO_x and CNF/SnO_x/SC films. At first, using CNF as substrate and LiOH adjusting the alkalinity, core/sheath structural SnO₂ nanosheets homogeneously grown on CNF (CNF/SnO₂) is fabricated under hydrothermal condition. One batch of CNF/SnO₂ is heated at 700 °C in N₂ atmosphere. The core/sheath structure of CNF/SnO₂ is disappeared, but SnO₂ nanosheets are reduced by a part of CNF and converted to spherical Sn submicron particles. Meanwhile, the surface of CNF becomes smooth again but its diameter decreases from 300 nm (Figure S2 in Supporting Information) to the 260 nm after carbothermal reduction (estimated by their SEM/TEM images shown in Figure 2 and Figure 3). The other batch of CNF/SnO₂ film is proceeded to be coated by spongy carbon assisted with glucose via hydrothermal process again. In subsequent heat treatment at 700 °C under N₂ atmosphere, SnO₂ is also reduced to form spherical Sn submicron particles but the SC with porous structure still remain on CNF in the final product of CNF/SnO₂/SC. The as-produced SnO_x submicron particles are fixed on the

core/sheath CNF/SC. It should be noted that the as-produced metallic tin will be oxidized in air atmosphere and covered by a passivation layer of SnO_2 . Thus, the final products after heat-treatment are named as CNF/ SnO_x and CNF/ SnO_x /SC, respectively.

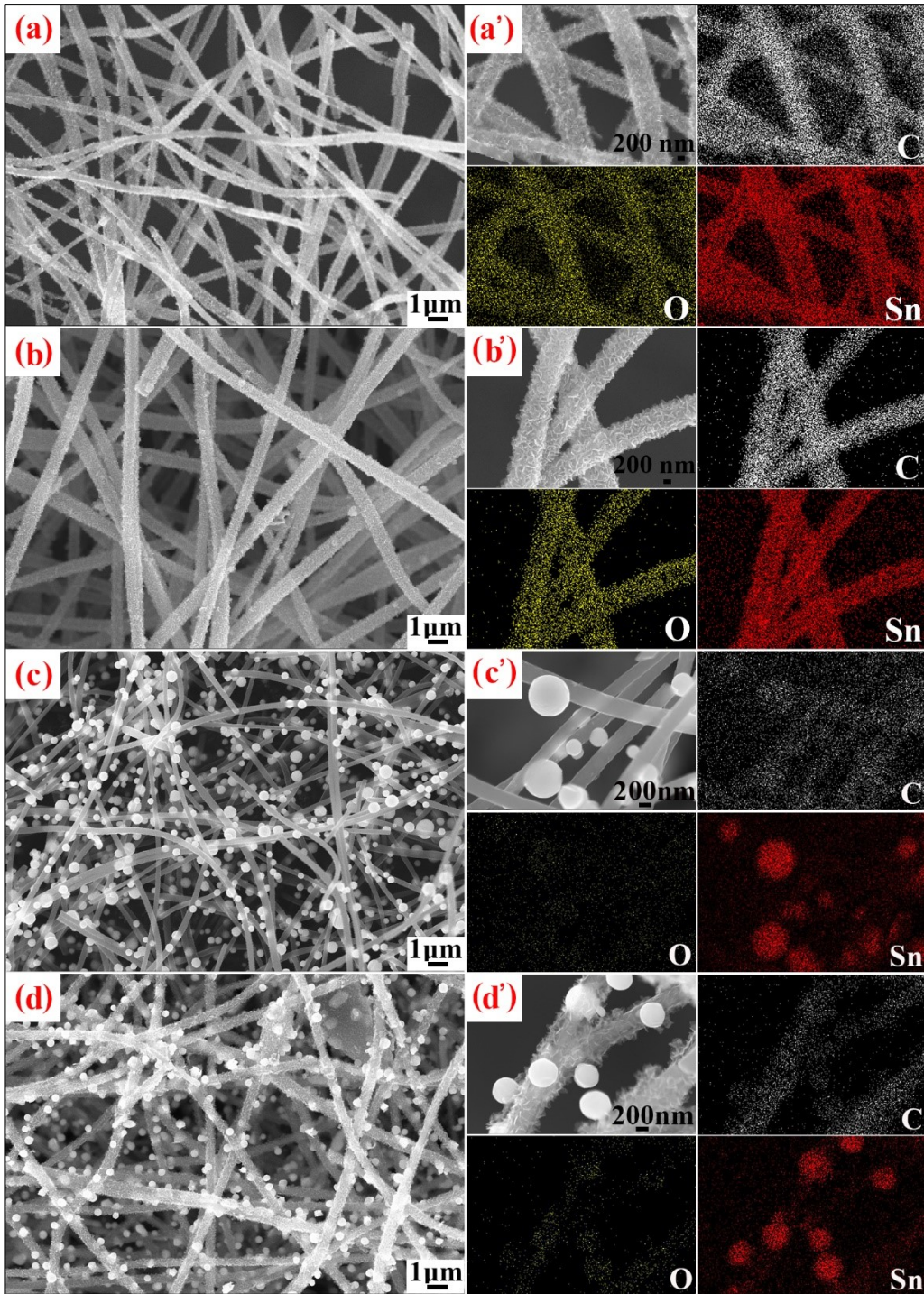


Figure 2. The SEM and elemental mapping images of CNF/SnO₂ (a, a'), CNF/SnO₂/SC (b, b'), CNF/SnO_x (c, c') and CNF/SnO_x/SC (d, d').

Figure 2 presents the SEM and elemental mapping images of the flexible films of CNF/SnO₂, CNF/SnO₂/SC, CNF/SnO_x and CNF/SnO_x/SC. Under hydrothermal condition, the as-produced SnO₂ nanosheets are tightly grown around the CNF to form core/sheath structural CNF/SnO₂ (Figure 2a). Sn, C and O elements are homogeneously dispersed on the fibers (Figure 2a'). The core/sheath structure of CNF/SnO₂ is disappeared after carbothermal reduction. CNF with smooth surface is reappeared, and spherical Sn submicron particles are fixed on CNF network. The as-produced CNF/SnO_x sample presents the CNF fiber with diameter of 200 – 400 nm and SnO_x particle sizes are range of 300-1000 nm (Figure 2c, 2c'). The elemental mapping images of CNF/SnO_x reveal C element on CNF and Sn element on spherical particles (Figure 2c'). The other batch of CNF/SnO₂ is coated by spongy carbon after hydrothermal process again, and the fiber diameter in CNF/SnO_x/SC sample increases to more than 460 nm (Figure 2d, 2d'). The product CNF/SnO₂/SC is still flexible film and C, O and Sn elements are homogeneously dispersed on the fibers (Figure 2b and 2b'). In subsequent carbothermal reduction, spherical Sn submicron particles are fixed on CNF network but the SC remains on fibers (Figure 2d). C and Sn elements are homogeneously dispersed on the fibers and particles, respectively (Figure 2d'). For comparison, SnO_x/C sample without CNF supporting presents aggregated crystal morphology in Figure S3 (in Supporting Information).

The crystalline structures of CNF/SnO₂, CNF/SnO₂/SC, CNF/SnO_x and CNF/SnO_x/SC films analysed by XRD are shown in Figure 3a and 3b. The diffraction peaks observed in CNF/SnO₂ and CNF/SnO₂/SC films all index to the rutile SnO₂

(JCPDS No.41-1445). The characteristic diffraction peaks observed at 26.5°, 33.9°, 37.8°, 51.9° are assigned to the crystal planes of (110), (101), (200) and (211), respectively. After post-heating treatment, the crystal phases of CNF/SnO₂ and CNF/SnO₂/SC are changed. Most diffraction peaks of CNF/SnO_x are assigned to metallic Sn (JCPDS No.04-0673), and there is a broad peak at the center of 22° (2θ) attributing to the typical amorphous carbon structure of CNF. The XRD patterns of CNF/SnO_x/SC are composed of metallic Sn, SnO₂ (JCPDS No.41-1445) and trace amounts of SnO (JCPDS No.72-1012). The control sample SnO_x/C presents almost the same XRD pattern with CNF/SnO_x/SC (Figure S4 in Supporting Information).

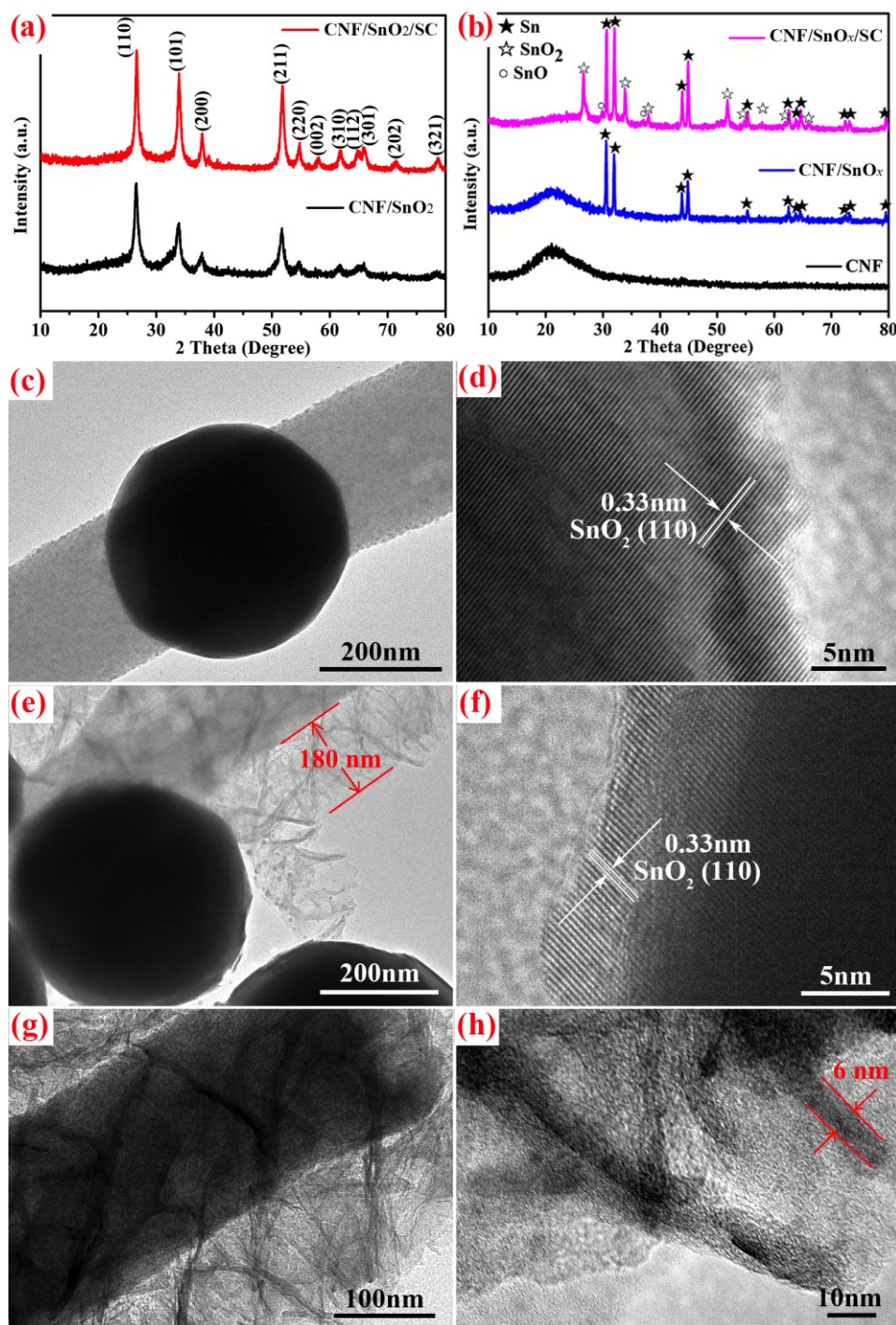


Figure 3. XRD patterns (a, b) of samples; TEM images of CNF/SnO_x (c, d) and CNF/SnO_x/SC (e-h).

The crystal structures of CNF/SnO_x and CNF/SnO_x/SC further analyzed using TEM and HRTEM are shown in Figure 3c-3h. It can be seen that the typical fiber with diameter of 260 nm and spherical particles (400 nm) in both samples (Figure 3c and 3e). The surface of the CNF and SnO_x particle are very smooth in CNF/SnO_x

sample (Figure 3c). The HRTEM image of CNF/SnO_x reveals a clear lattice fringe of 0.33 nm which corresponds to the (110) plane of SnO₂ (Figure 3d). CNF/SnO_x/SC sample presents the same crystal morphology of SnO_x particle with CNF/SnO_x, but there are SC sheathed on CNF and the length of the SC is about 180 nm (Figure 3e). The SC is porous and amorphous with a few nanometers in thickness, and it will play the role in buffering the pulverization and volumetric change of SnO_x during lithiation/delithiation (Figure 3h).

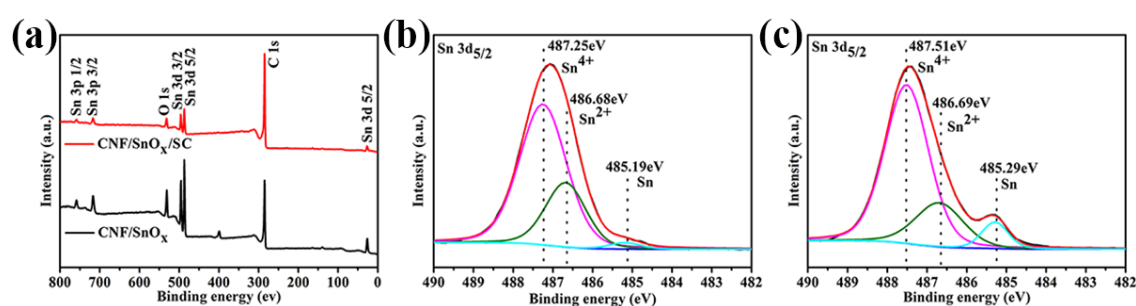


Figure 4. XPS survey spectra (a); high-resolution Sn 3d_{5/2} spectra of CNF/SnO_x (b) and CNF/SnO_x/SC (c).

The surface chemical composition of CNF/SnO_x and CNF/SnO_x/SC evaluated by XPS are displayed in Figure 4. The survey spectra present C, O and Sn elements in CNF/SnO_x and CNF/SnO_x/SC samples. The typical C 1s peak can be observed at the center of 284.6 eV, and the presence of oxygen species observed near 531 eV indicates that tin oxide is formed on the surface of tin particles (Figure S5a-b in Supporting Information). The high-resolution Sn XPS of samples are shown in Figure S5c in Supporting Information, including two main peaks near 494.5 eV (Sn 3d_{3/2} for SnO₂) and 486.0 (Sn 3d_{5/2} for SnO₂) and two weak peaks close to 492.4 eV (Sn 3d_{3/2} for Sn) and 484.1 eV (Sn 3d_{5/2} for Sn).²³ The high-resolution Sn 3d_{5/2} spectra are fitted using PeakFit software and the corresponding fitted results are shown in Figure

4b-4c. It can be seen that the surface of both samples includes the majority species of Sn^{4+} and Sn^{2+} and the minority of Sn^0 .²⁴ Considering the detection depth of XPS, the XPS result of Figure 4b-4c implies that a passivation layer of tin oxide is grown on metallic tin. Based on the results of XRD and XPS, it can be deduced that the Sn/SnO_2 core/shell structure is existed in CNF/SnO_x and $\text{CNF}/\text{SnO}_x/\text{SC}$ samples though it is hard to be distinguished in their TEM images.

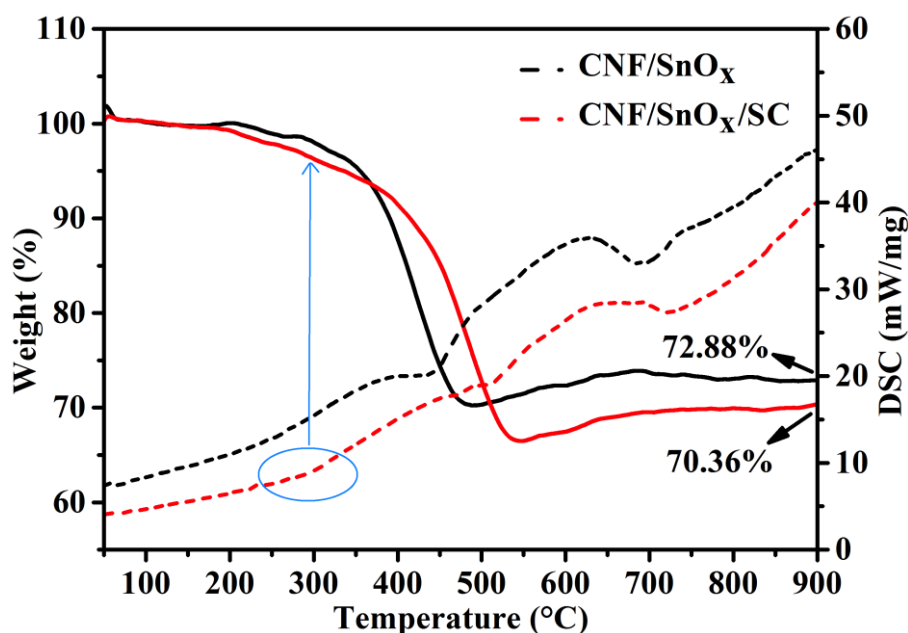


Figure 5. TG/DSC curves of CNF/SnO_x and $\text{CNF}/\text{SnO}_x/\text{SC}$ samples.

The thermal behavior of CNF/SnO_x and $\text{CNF}/\text{SnO}_x/\text{SC}$ samples are analyzed by TG/DSC and the curves are shown in Figure 5. CNF/SnO_x shows the exothermic peak at 448 °C attributed to the burning of CNF in O_2 atmosphere, and the consequent weight loss is about 29wt% till 482 °C. The weight loss of $\text{CNF}/\text{SnO}_x/\text{SC}$ sample starts from 200 °C under O_2 atmosphere which corresponds to a weak exothermic peak at the center of 300 °C, because highly porous spongy carbon is easier oxidized by pure O_2 . Furthermore, spongy carbon as sheath covered CNF in $\text{CNF}/\text{SnO}_x/\text{SC}$ sample hinders the oxidation of CNF to some degree. The exothermic peak of

CNF/SnO_x/SC shifts to 500 °C, and the consequent weight loss is close to 33wt% till 538 °C. Subsequently, CNF/SnO_x and CNF/SnO_x/SC present exothermic peaks at 681 °C and 726 °C, respectively, resulting from the oxidation process of metallic tin in both samples. Because of the passivation layer SnO₂ formed on the particle surface, it prevents the oxidation of the inner side of metallic tin even at high temperature. Finally, the retention about 73wt% and 70wt% is observed in CNF/SnO_x and CNF/SnO_x/SC samples till 900°C, respectively. The EDX and CHN elemental analysis results are collected in this work. C, O, N and Sn elements are detected by EDX (Figure S6 in Supporting Information). However, the C:N:O ratio collected by EDX is deviated from that by CHN elemental analysis. Based on the quantity evaluated by CHN elemental analysis and TG analysis, the calculated C:O:N:Sn weight ratio is 24.3%:2.2%:6.7%:66.8% in CNF/SnO_x sample and 27.0%:2.3%:6.9%:63.8% in CNF/SnO_x/SC sample. The elemental analysis show the reasonable ratio in both samples.

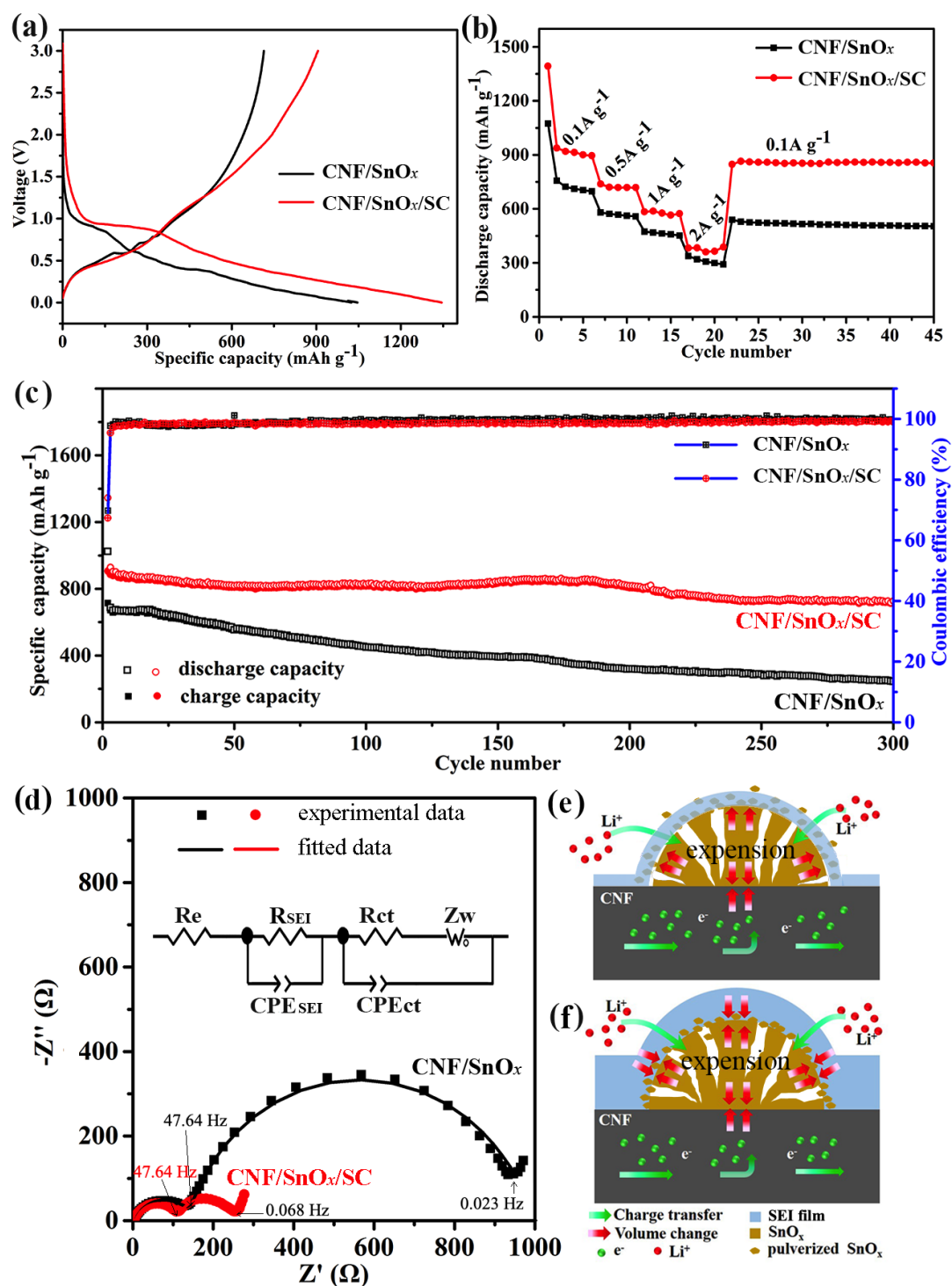


Figure 6. The 1st discharge/charge curves (a), rate curves (b), cyclic curves (c), the Nyquist plots (d), and the schemed energy-storage mechanisms (e, f) of CNF/SnO_x and CNF/SnO_x@C lithiated electrodes.

3.2 Electrochemical Performances of the Hybrid Composites

The cyclic voltammograms (CV) curves of CNF/SnO_x and CNF/SnO_x/SC are shown in Figure S7 (in Supporting Information). In the first cathodic process, CNF/SnO_x and CNF/SnO_x/SC show two kinds of peaks. The broad peaks between 1.0 V and 0.5 V are attributed to the lithiation of SnO₂ ($\text{Li}^+ + \text{SnO}_2 + 4\text{e}^- \rightarrow \text{Sn} + 2\text{Li}_2\text{O}$) and the formation of solid-electrolyte-interphase (SEI).^{25,26} The above two processes are irreversible and absent in the subsequent CV cycles. A broad peak in 0.3 - 0.001 V is attributed to Li-Sn alloying ($x\text{Li} + \text{Sn} + x\text{e}^- \leftrightarrow \text{Li}_x\text{Sn}$), which is reversible and can still be observed in the following cycles.^{28,29} In the subsequent anodic scan of CNF/SnO_x and CNF/SnO_x/SC, the peaks between 0.5 V and 0.8 V are attributed to the dealloying of Li_xSn. Moreover, the particular cathodic peak at 0.85 V and anodic peak at 1.25 V observed in CNF/SnO_x/SC sample are attributed to the lithiation/delithiation of CNF.²⁹ From the 2nd to the 6th cycle, the CV profiles of CNF/SnO_x/SC samples display higher overlapped degree than those of CNF/SnO_x, illustrating highly reversible redox reactions in the former.

Galvanostatic charge/discharge measurements are recorded in Figure 6a-6c. In this work, the specific capacity is calculated based on the total mass of the binder-free film. Figure 4a depicts the first discharging/charging profiles at 0.1 A g⁻¹. CNF/SnO_x reveals discharging capacity of 1024.0 mAh g⁻¹ and charging capacity of 714.0 mAh g⁻¹, while the CNF/SnO_x/SC electrode displays a higher discharging capacity of 1345.1 mAh g⁻¹ and charging capacity of 906.1 mAh g⁻¹. The irreversible capacity at the first cycle is ascribed to the formation of SEI and other irreversible reaction. The difference of rate capability between the CNF/SnO_x and CNF/SnO_x/SC electrodes are exhibited in Figure 6b. CNF/SnO_x/SC presents much better rate performance than CNF/SnO_x. At 0.1, 0.5, 1 and 2 A g⁻¹, the discharge capacities are 1074.1, 580.0,

473.5 and 337.9 mAh g⁻¹ collected in CNF/SnO_x electrode, as well as 1393.0, 738.2, 583.6 and 382.6 mAh g⁻¹ in CNF/SnO_x/SC electrode, respectively. Especially, the capacity of CNF/SnO_x/SC can be recovered to 847.9 mAh g⁻¹ when the current density returns to 0.1 A g⁻¹, in comparison, CNF/SnO_x is only 538.8 mAh g⁻¹. The conductive channel of CNF and porous structure of SC synergistically improve the rate performance of CNF/SnO_x/SC.

Long cyclic performance of samples is important for evaluating the practical applications. Figure 6c presents the cyclic curves and columbic efficiency of CNF/SnO_x and CNF/SnO_x/SC at 0.1 A g⁻¹. The capacity of CNF/SnO_x gradually decays to 244.6 mAh g⁻¹ after 300 cycles, but the discharge capacity of CNF/SnO_x/SC can be maintained at 726.9 mAh g⁻¹ with columbic efficiency of 99.45 % after 300 cycles. The intermediate product CNF/SnO₂ shows low specific discharge capacity (about 600 mAh g⁻¹ at the 1st cycle) and poor cyclic performance (157 mAh g⁻¹ at the 200th cycle) (Figure S8 in Supporting Information). The comparison sample SnO_x/C also shows rapid capacity fading (198 mAh g⁻¹ at the 100th cycle) (Figure S9 in Supporting Information). Furthermore, other control sample SnO₂ with the similar grain size is synthesized. It is micron sized particles (0.5 ~1.5 μm) as shown in SEM and TEM images (Figure S10a-10c). SnO₂ sample can deliver high specific capacity of 1346 mAh g⁻¹ with a coulombic efficiency of 61.2%, but the capacity rapidly decreases to 50 mAh g⁻¹ at the 100th cycle due to the serious pulverization of SnO₂ particles. According to the abovementioned electrochemical performance of tin-based anode materials with different kinds of crystal morphologies, it can be concluded that elastic CNF and porous SC effectively enhance the stability and conductivity of submicron sized SnO_x particles during lithiation/delithiation process.

To better understand the conductive behavior of CNF/SnO_x and CNF/SnO_x/SC samples, the Nyquist plots of the electrodes before cycling (Fig. S11 in Supporting information), it can be seen that both samples present similar Nyquist plots before cycling. Furthermore, the Nyquist plots of the electrodes at the 2nd discharged state are collected as shown in Figure 6d, and the inset graph is the corresponding equivalent circuit model. Each Nyquist plot consists of a short origin intercept in the high frequency, two semicircles and a sloping line, which can be analyzed by the components of solution resistance (R_e) of the cell, the resistance of SEI (R_{SEI}), the charge transfer resistance (R_{ct}) and Warburg impedance (Z_w), etc.^{31,32} By using the equivalent circuit, the aforementioned parameters for Nyquist plots are listed in Table S1 (in Supporting Information). The reliability factors (χ^2) are near 10^{-4} , indicating the fitting data are reliable. Two samples exhibit similar value of R_e . CNF/SnO_x presents larger R_{SEI} (134.8 Ω) and R_{ct} (843.8 Ω) than CNF/SnO_x/SC (109.9 and 124.5 Ω , respectively). It confirms that the spongy carbon effectively improves the conductivity of the submicron SnO_x particles.

3.3 Discharge-Charge Mechanism of the Hybrids

Figure 6e and 6f are the schematic electrochemical behavior and mechanism diagrams of the CNF/SnO_x and CNF/SnO_x/SC electrodes after charging-discharging process. CNF and the SC provide fast channel for the electron transport in this design. Since huge volume expansion of the submicron SnO_x particles arises from the insertion of Li ions, the SnO_x particles are pulverized and peeled off resulting in a capacity fading in CNF/SnO_x sample. However, the spongy carbon in CNF/SnO_x/SC sample can hinder the pulverization and peeling of the submicron SnO_x particles, because the as-produced SEI films covers the mixture of SnO_x particles, spongy

carbon and CNF. And thus, CNF/SnO_x/SC sample presents much better cyclic performance than CNF/SnO_x sample.

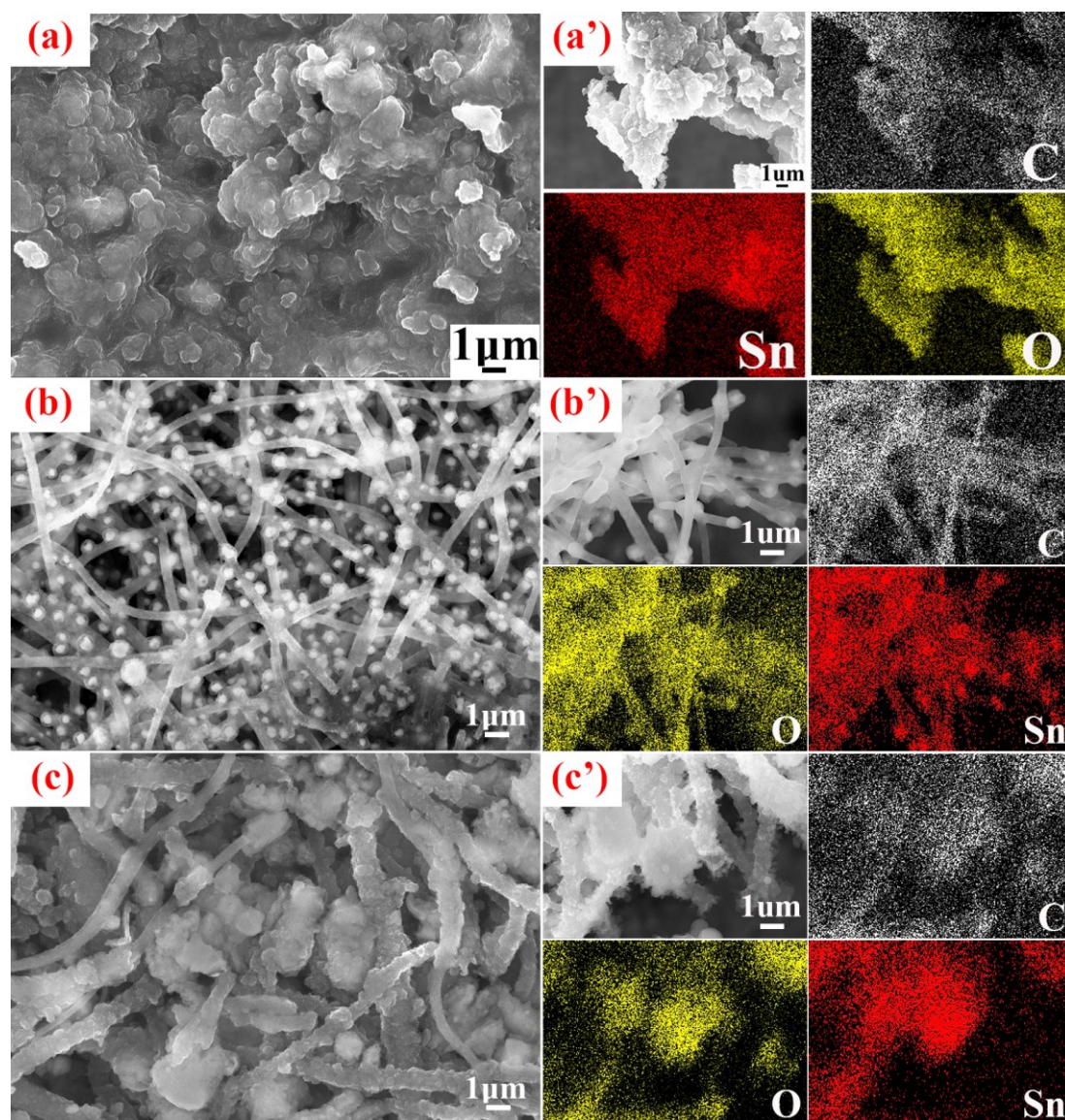


Figure 7. SEM and elemental mapping images of SnO_x/C (a, a'), CNF/SnO₂ (b, b') and CNF/SnO_x/SC (c, c') electrodes at the first discharging state.

The SEM and elemental mapping images of the control sample SnO_x/C, CNF/SnO_x, and CNF/SnO_x/SC film electrodes after the first discharging are displayed in Figure 7 to show the morphology changes. The lithiated SnO_x/C electrode presents serious aggregation of particles (Figure 7a). The diameter of CNF in lithiated

CNF/SnO_x electrode is slightly bigger than its original size because CNF involves in lithiation to some extent, and the pulverized SnO_x particles are covered by SEI film and separately dispersed in CNF network (Figure 7b). The relative XRD patterns indicate that the typical double peaks of metallic tin are combined to single peak due to lithium-tin alloying (Figure S12a in Supporting Information). For the lithiated CNF/SnO_x/SC electrode, some of lithiated SnO_x micron particles covered by SEI films form an aggregation of the mixed particles as shown in Figure 7c, furthermore the XRD patterns of the lithiated CNF/SnO_x/SC electrode shows a broaden peak at the center of 30° assigned to amorphous carbon (Figure S12b in Supporting Information). Considering the structure of micron sized tin particles staying on CNF and spongy carbon, all of them will be mixed together, that is, the as-produced SEI film covers SnO_x particles, spongy carbon and CNF because all of them involve in lithiation to different extent and form SEI films. And thus, the diameter of CNF in CNF/SnO_x/SC electrode at the first discharging state increases to 1 μm because SEI films cover on lithiated SnO_x particles, spongy carbon and CNF together. In the integrated structure of CNF/SnO_x/SC, submicron SnO_x particles as active material provide high capacity, meanwhile, CNF and spongy carbon provide conductive channel and buffer zone to improve the electrochemical properties of SnO_x.

4. Conclusion

In summary, the integrated structure of CNF/SnO_x/SC has been successfully synthesized by hydrothermal and carbothermal reduction treatment. SnO₂ nanosheets that coated by spongy carbon are homogeneously grown on the substrate of CNF in hydrothermal field. During carbothermal reduction, SnO₂ nanosheets convert to submicron tin oxide particles and hollow spongy carbon remains on CNF, and thus

the structure of the submicron tin oxide particles fixed on core/sheath structural carbon nanofibers/spongy carbon is successfully produced. CNF/SnO_x/SC flexible film has been used as binder-free anode material for LIBs. CNF/SnO_x/SC composite electrode delivers capacity of 1393.0, 738.2, 583.6 and 382.6 mAh g⁻¹ at 0.1, 0.5, 1 and 2 A g⁻¹, respectively. For 300 cycles at 0.1 A g⁻¹, CNF/SnO_x/SC sample maintains the capacity of 726.9 mAh g⁻¹ with columbic efficiency of 99.45 %. Herein, the pulverization and peeling of SnO_x particles is effectively hindered because CNF and SC cooperatively provide conductive channel and buffer zone.

Acknowledgements

The authors greatly appreciate the financial support of the Natural Science Foundation of Jiangsu Province (Grant No. BK20160409, BK20161267).

References

- (1) C. Heubner, T. Liebmann, K. Voigt, M. Weiser, B. Matthey, N. Junker, C. Lämmel, M. Schneider, A. Michaelis, Scalable Fabrication of Nanostructured Tin Oxide Anodes for High-Energy Lithium-Ion Batteries, *ACS Appl. Mater. Interfaces* **2018**, 10, 32, 27019–27029.
- (2) Z. Li, J.W. Zhang, J. Shu, J.P. Chen, C.H. Gong, J.H. Guo, L.G. Yu, J.W. Zhang, Carbon Nanofibers with Highly Dispersed Tin and Tin Antimonide Nanoparticles: Preparation via Electrospinning and Application as the Anode Materials for Lithium-Ion Batteries, *J. Power Sources* **2018**, 381, 1–7.
- (3) W.J. Dong, J.J. Xu, C. Wang, Y. Lu, X.Y. Liu, X. Wang, X.T. Yuan, Z. Wang, T.Q. Lin, M. L. Sui, I-W. Chen, F.Q. Huang, A Robust and Conductive Black Tin

Oxide Nanostructure Makes Efficient Lithium-Ion Batteries Possible. *Adv. Mater.* **2017**, 29, 1700136.

(4) N. Zhang, Y.Y. Wang, M. Jia, Y.C. Liu, J.Z. Xu, L.F. Jiao, F.Y. Cheng, Ultrasmall Sn Nanoparticles Embedded in Spherical Hollow Carbon for Enhanced Lithium Storage Properties, *Chem. Commun.* **2018**, 54, 1205–1208.

(5) C.F. Deng, Y. Liu, Z.P. Lu, C. Ma, T. Ge, W. Li, G. Yang, The Effect of Passivation Film in Preparation 3D Structural Carbon Paper/Tin Oxide@carbon as Freestanding Anode for Lithium-ion Batteries, *Appl. Surf. Sci.* **2018**, 435, 1307–1313.

(6) F. Wang, L. Chen, C.F. Deng, H.T. Ye, X.F. Jiang, G. Yang, Porous Tin Film Synthesized by Electrodeposition and the Electrochemical Performance for Lithium-ion Batteries, *Electrochim. Acta* **2014**, 149, 330–336.

(7) Y.F. Deng, C.C. Fang, G.H. Chen, The Developments of SnO₂/graphene Nanocomposites as Anode Materials for High Performance Lithium Ion Batteries: A Review, *J. Power Sources* **2016**, 304, 81–101.

(8) H. Woo, S. Wi, J. Kim, J. Kim, S. Lee, T. Hwang, J. Kang, J. Kim, K. Park, B. Gil, Complementary Surface Modification by Disordered Carbon and Reduced Graphene Oxide on SnO₂ Hollow Spheres as an Anode for Li-ion Battery, *Carbon* **2018**, 129, 342–348.

(9) D.D. Liu, Z. Kong, X.H. Liu, A.P. Fu, Y.Q. Wang, Y.G. Guo, P.Z. Guo, H.L. Li, X.S. Zhao, Spray-Drying-Induced Assembly of Skeleton-Structured SnO₂/Graphene Composite Spheres as Superior Anode Materials for High Performance Lithium-Ion Batteries, *ACS Appl. Mater. Interfaces* **2018**, 10, 2515–2525.

(10) Y. Cheng, Q. Li, C.L. Wang, L.S. Sun, Z. Yi, L.M. Wang, Large-Scale Fabrication of Core-Shell Structured C/SnO₂ Hollow Spheres as Anode Materials with Improved Lithium Storage Performance, *Small* **2017**, 13, 1701993.

- (11) W.H. Xie, L.L. Gu, F.Y. Xia, B.L. Liu, X.Y. Hou, Q. Wang, D.Q. Liu, D.Y. He, Fabrication of Voids-Involved SnO₂@C Nanofibers Electrodes with Highly Reversible Sn/SnO₂ Conversion and Much Enhanced Coulombic Efficiency for Lithium-Ion Batteries, *J. Power Sources* **2016**, 327, 21–28.
- (12) V.A. Agubra, L. Zuniga, D. Flores, H. Campos, J. illarreal, M. Alcoutlabi, A Comparative Study on the Performance of Binary SnO₂/NiO/C and Sn/C Composite Nanofibers as Alternative Anode Materials for Lithium Ion Batteries, *Electrochim. Acta* **2017**, 22, 608–621.
- (13) B. Joshi, E. Samuel, H.S. Jo, Y. Kim, S. Park, M.T. Swihart, W.Y. Yoon, S.S. Yoon, Carbon Nanofibers Loaded with Carbon Nanotubes and Iron Oxide as Flexible Freestanding Lithium-Ion Battery Anodes, *Electrochim. Acta* **2017**, 253, 479–488.
- (14) G.-H. An, D.-Y. Lee, Y.-J. Lee, H.-J. Ahn, Ultrafast Lithium Storage Using Antimony-Doped Tin Oxide Nanoparticles Sandwiched between Carbon Nanofibers and a Carbon Skin, *ACS Appl. Mater. Interfaces* **2016**, 8, 30264–30270.
- (15) B. Zhang, F.Y. Kang, J.-M. Tarascon, J.-K. Kim, Recent Advances in Electrospun Carbon Nanofibers and Their Application In Electrochemical Energy Storage, *Prog. Mater. Sci.* **2016**, 76, 319–380.
- (16) C.A. Bonino, L.W. Ji, Z. Lin, O. Toprakci, X.W. Zhang, S. A. Khan, Electrospun Carbon-Tin Oxide Composite Nanofibers for Use as Lithium Ion Battery Anodes, *ACS Appl. Mater. Interfaces* **2011**, 3, 2534–2542.
- (17) M.Z. Zou, J.X. Li, W.W. Wen, Y.B. Lin, H. Lai, Z.G. Huang, Free-Standing Anode of N-doped Carbon Nanofibers Containing SnO_x For High-Performance Lithium Batteries, *Mater. Res. Bull.* **2014**, 60, 868–871.
- (18) G. Yang, Y.H. Li, H.M. Ji, H.Y. Wang, P. Gao, L. Wang, H.D. Liu, J. Pinto, X.F. Jiang, Influence of Mn Content on the Morphology and Improved Electrochemical

Properties of $\text{Mn}_3\text{O}_4/\text{MnO}@$ carbon Nanofiber as Anode Material for Lithium Batteries, *J. Power Sources* 2012, 216, 353–362.

(19) M.X. Zhao, Y. Liu, J.L. Jiang, C. Ma, G. Yang, F. Yin, Y. Yang, Sheath/Core Hybrid FeCO_3 /Carbon Nanofibers as Anode Materials for Superior Cycling Stability and Rate Performance, *ChemElectroChem* 2017, 4, 1450–1456.

(20) G.-H. An, H.-J. Ahn, Carbon Nanofiber/Cobalt Oxide Nanopyramid Core-shell Nanowires for High-Performance Lithium-Ion Batteries, *J. Power Sources* 2014, 272, 828–836.

(21) J.L. Jiang, C. Ma, Y. Yang, J. Ding, H. Ji, S. Shi, G. Yang, Synergetic Interface between $\text{NiO}/\text{Ni}_3\text{S}_2$ Nanosheets and Carbon Nanofiber as Binder-Free Anode for Highly Reversible Lithium Storage, *Appl. Surf. Sci.* 2018, 441, 232–238.

(22) T. Wang, H.G. Li, S.J. Shi, T. Liu, G. Yang, Y.M. Chao, F. Yin, 2D Film of Carbon Nanofibers Elastically Astricted MnO Microparticles: A Flexible Binder-Free Anode for Highly Reversible Lithium Ion Storage, *Small* 2017, 13, 1604182.

(23) J.J. Ding, Z.P. Lu, M.M. Wu, C. Liu, Y. Yang, H.M. Ji, G. Yang, Carbon coated SnO_2 particles stabilized in the elastic network of carbon nanofibers and its improved electrochemical properties. *Mater. Chem. Phys.* 2018, 215, 285–292.

(24) C.D. Gu, Y.J. Mai, J.P. Zhou, Y.H. You, J.P. Tu, Non-Aqueous Electrodeposition of Porous Tin-Based Film as an Anode for Lithium-Ion Battery, *J. Power Sources* 2012, 214, 200–207.

(25) Y.Y. Cheng, J.F. Huang, H. Qi, L.Y. Cao, J. Yang, Q. Xi, X.M. Luo, K. Yanagisawa, J.Y. Li, Adjusting the Chemical Bonding of $\text{SnO}_2@$ CNT Composite for Enhanced Conversion Reaction Kinetics, *Small* 2017, 13, 1700656.

- (26) J.H. Sun, L.H. Xiao, S.D. Jiang, G.X. Li, Y. Huang, J.X. Geng, Fluorine-Doped SnO₂@Graphene Porous Composite for High Capacity Lithium-Ion Batteries. *Chem. Mater.* **2015**, *27*, 4594–4603.
- (27) L.P. Wang, Y. Leconte, Z. Feng, C. Wei, Y. Zhao, Q. Ma, W. Xu, S. Bourrioux, P. Azais, M. Srinivasan, Z.J. Xu, Novel Preparation of N-doped SnO₂ Nanoparticles via Laser-assisted Pyrolysis: Demonstration of Exceptional Lithium Storage Properties. *Adv. Mater.* **2017**, *29*, 1603286.
- (28) V.A. Agubra, L. Zuniga, D.D. L. Garza, L. Gallegos, M. Pokhrel, M. Alcoutlabi, Forcespinning: A New Method for the Mass Production of Sn/C Composite Nanofiber Anodes for Lithium Ion Batteries. *Solid State Ionics* **2016**, *286*, 72–82.
- (29) S.Z. Liang, X.F. Zhu, P.C. Lian, W.S. Yang, H.H. Wang, Superior Cycle Performance of Sn@C/graphene Nanocomposite as an Anode Material for Lithium-ion Batteries. *J. Solid State Chem.* **2011**, *184*, 1400–1404.
- (30) T. Wang, S.J. Shi, Y.H. Li, M.X. Zhao, X.F. Chang, D. Wu, H.Y. Wang, L.M. Peng, P. Wang, G. Yang, The Study of Microstructure Change of Carbon Nanofibers as Binder-Free Anode for High-Performance Lithium-Ion Batteries. *ACS Appl. Mater. Interfaces* **2016**, *8*, 33091–33101.
- (31) H. Li, X.J. Huang, L.Q. Chen, Electrochemical Impedance Spectroscopy Study of SnO and Nano-SnO Anodes in Lithium Rechargeable Batteries. *J. Power Sources* **1999**, *81*, 340–345.
- (32) D. Andre, M. Meiler, K. Steiner, C. Wimmer, T. Soczka-Guth, D.U. Sauer, Characterization of High-power Lithium-ion Batteries by Electrochemical Impedance Spectroscopy. I. Experimental Investigation. *J. Power Sources* **2011**, *196*, 5334–5341.